More than just a wrinkle: a wave-like pattern in U_g versus L_z from *Gaia* data

Jennifer K. S. Friske[1]★ and Ralph Schönrich [2,3]

[1]*Fakultät für Physik, Ludwig-Maximilians-Universität, Schellingstr. 4, D-80799 München, Germany*
[2]*Rudolf Peierls Centre for Theoretical Physics, Clarendon Laboratories, University of Oxford, OX1 3PU Oxford, UK*
[3]*Mullard Space Science Laboratory, University College London, Holmbury St Mary, Dorking, Surrey, RH5 6NT, UK*

ABSTRACT

We present a newly found wave-like pattern in mean Galactocentric radial velocity $\overline{U}_g$ versus guiding centre radius R_g or angular momentum L_z of stars in the RV subsample of *Gaia* DR2. The short-wave pattern has a wavelength of order 1.2 kpc in R_g or 285 kpc km s^{-1} in L_z. The pattern shows only weak changes with Galactocentric radius R and little change in strength in particular with the vertical energy E_z of the stars or the distance to the Galactic plane $|z|$. The pattern is to first order symmetric around the plane, i.e. has no significant odd terms in z. There is a weak phase shift with the pattern moving towards slightly lower L_z (i.e. trailing) with $|z|$ and E_z. However, we observe a highly significant phase shift in Galactic azimuth ϕ, which is different for different peaks. The peak around $L_z \sim 2100$ kpc km s^{-1} only shows a weak change with ϕ, while the rest of the pattern shows a clearly detectable shift of $dL_z/d\phi = (200 \pm 22)$ kpc km s^{-1} rad^{-1}. If we consider all peaks to belong to the same pattern, this would suggest a wavenumber $m = 4$. We further find that the wave-like pattern in U_g appears to be related to the $\overline{W}$ versus L_z pattern detected in *Gaia* DR1. A comparison of the $\overline{U}_g$–L_z wave pattern with changes of $\overline{U}_g$ versus R, which have been previously discussed, suggests that the latter can be understood as just the $\overline{U}_g$–L_z pattern washed out by blurring (i.e. orbital excursions around their guiding centre) of disc stars.

Key words: stars: kinematics and dynamics – Galaxy: disc – Galaxy: kinematics and dynamics – solar neighbourhood – Galaxy: structure.

1 INTRODUCTION

From its first data release, the *Gaia* satellite mission (Gaia Collaboration 2016a) has been providing a stunning, unprecedented view on disc structure. In fact, we are only very slowly getting to grips with new features in phase space that were not fully anticipated in theoretical models. Given the great technological advance compared to its predecessor *Hipparcos* (Perryman et al. 1997), we can expect that *Gaia*'s data will reveal many surprising diagnostics of the disc structure and kinematics that are hidden in plain sight. In this paper, we will discuss a newly found dependence of the mean radial velocity $\overline{U}_g$ on angular momentum L_z, which exhibits a strong wave-like pattern.

One example of beautiful surprises by *Gaia* has been the discovery of vertical substructure in the motion of disc stars. While *Hipparcos* had just delivered very tentative evidence for the Galactic warp (Dehnen 1998), molecular gas observations and star counts of bright stars (e.g. Drimmel, Smart & Lattanzi 2000; Drimmel & Spergel 2001; Reylé et al. 2009) have shown that the Sun is quite

close to the line of nodes of a large-scale outer disc warp. We should thus expect stars with large angular momenta to have a positive mean vertical velocity $\overline{W}$ relative to the disc. Instead of just confirming the tentative evidence of the Galactic warp in *Hipparcos* (Poggio et al. 2018; Schönrich & Dehnen 2018), already *Gaia* DR1 provided more than a quantification of the warp signal. It revealed the presence of a wave-like pattern with an amplitude of ~ 1 km s^{-1} of $\overline{W}$ versus L_z with a scale length of order 500 kpc km s^{-1} or ~ 2 kpc in guiding centre radius R_g (Schönrich & Dehnen 2018). This wave (confirmed later by Seabroke et al. 2018, on *Gaia* DR2) is likely connected to the much larger waves in the outer disc (Xu et al. 2015; Bergemann et al. 2018): the local amplitude should be a lot smaller due to the much larger local surface density compared to the outskirts of the disc. The most likely culprit is also known: the previous impact of the Sagittarius Dwarf Galaxy and its then a lot more massive dark matter halo, causing a wake in the halo (Weinberg 1995) and then the corrugated warp/wave pattern in the Galactic disc (D'Onghia et al. 2016; Laporte et al. 2018).

Related to this vertical wave structure, *Gaia* DR2 also brought the discovery of the phase-space spiral (Antoja et al. 2018) – a prominent spiral shape in the W–z plane (altitude z above or below the disc plane), which is particularly visible if one colours each bin

★ E-mail: j.friske@physik.lmu.de

by its mean (Galactocentric) azimuthal or radial velocity, $\overline{V}_g$ or $\overline{U}_g$. This spiral has been extensively scrutinised (Bland-Hawthorn et al. 2019) and readily explained with an impact of a companion galaxy and its resulting vertical impulse on the disc, very likely stemming from the last pericentric passage of the Sagittarius Dwarf Galaxy 500–800 Myr ago (Binney & Schönrich 2018; Darling & Widrow 2018; Laporte et al. 2019)

Here, we will show that there is a very clear wave-like pattern present in $\overline{U}_g$ versus L_z throughout the entire extent (spanning a diameter of more than 4 kpc) probed by the *Gaia* RV data set. This data set adds line-of-sight velocities to the *Gaia* astrometry and thus provides full 6D phase-space information for ∼7 million objects. In Section 3, we describe the data used for our evaluation and how the catalogue used was derived from the *Gaia* sample. In the following Section 4, we present the pattern and investigate its behaviour at different positions in the sample data range. We try to quantify the azimuthal phase shift in Section 4.2 by fitting a suitable function to our data and give an estimate for the involved wavenumbers. Section 4.3 then investigates correspondences between the $\overline{U}_g$–L_z pattern and the waves in $\overline{W}$ versus L_z, as well as the trends in $\overline{U}_g$ versus galactocentric radius R. Finally, we summarise our findings in Section 5.

2 COORDINATE FRAME AND DEFINITIONS

We use a standard right-handed coordinate system (U, V, W) for the velocities, where U is the component of motion towards the Galactic Centre (GC), V in the direction of Galactic rotation, and W quantifies the motion upwards, perpendicular to the plane. We distinguish between Galactocentric velocity components (U_g, V_g, W), which are measured in a cylindrical coordinate system in the rest frame of the GC, and heliocentric velocity components (U_h, V_h, W_h), which are measured in the Cartesian coordinate system relative to the motion of the Sun. That is, at the position of any star U_g points towards the Galactic central axis (and for comparison to the other tradition $U_g = -v_R$ and $V_g = v_\phi$), while U_h points parallel to the line Sun − central axis. Slightly inconsistent in sign and with the handedness of the coordinate system, we define the angular momentum $L_z = RV_g$, positive in the direction of disc rotation. We set the solar Galactocentric radius $R_0 = 8.27$ kpc, the total azimuthal velocity of the Sun $V_{g,\odot}$, and the local standard of rest velocity vector of the Sun $(U_\odot, V_\odot, W_\odot) = (11.1, 12.24, 7.25)$ km s^{-1}. These values have been taken from Schönrich (2012) and Schönrich, Binney & Dehnen (2010) in accordance with Gillessen et al. (2009) and McMillan (2017). The values thus imply a local circular speed $V_c = 238$ km s^{-1} and a solar value $L_{z,\odot} = 2067$ kpc km s^{-1}. For each star, we make use of Galactocentric cylindrical coordinates, where $R = \sqrt{x^2 + y^2}$ denotes the in-plane Galactocentric radius and (x, y, z) are the coordinates in the Galactocentric Cartesian frame with the GC at $R = x = y = z = 0$, x in the radial direction outwards, y in the azimuthal direction, and z perpendicular to the Galactic plane. We denote Galactic longitude and latitude with (l, b). An important quantity in our analysis is the azimuth of a star, i.e. the in-plane angle between the connection lines Sun–GC and GC–star. The azimuth is taken positive in the direction of rotation with $\phi = 0$ at the solar position.

3 DATA

In this study, we make use of the *Gaia* RV sample (Cropper et al. 2018; Gaia Collaboration 2018b), which has been published as

a part of *Gaia* DR2 (Gaia Collaboration 2018a). Descriptions of the *Gaia* spacecraft and of its onboard spectrograph can be found in *Gaia* Collaboration (2016b) and Sartoretti et al. (2018). To derive the 6D phase-space information, we employ the astrometric information from *Gaia* DR2, which provides proper motions and parallax measurements (Arenou et al. 2018; Lindegren et al. 2018). For the sake of simplicity, we will stick with the position–velocity phase space for our considerations; however, a study of the *Gaia* DR2 sample in action space can be found in Trick, Coronado & Rix (2019), which also displays some of the ridges and undulations under concern. To provide distances for the sample, we use the distance expectation values from Schönrich, McMillan & Eyer (2019), which were derived with the method of Schönrich & Aumer (2017). Using the expectation values for the distance has the advantage that the expectation values of velocity components should be unbiased. The distances have been extensively tested and calibrated the *Gaia* parallax offset $\delta p = (0.054 \pm 0.06)$ mas (Gaia parallaxes are too small), using the method of Schönrich, Binney & Asplund (2012). The implied offset is substantially (a factor 2) larger than that estimated from the *Gaia* quasar sample in Lindegren et al. (2018). However, the quasar sample is a lot fainter, has a different colour distribution, and has generally zero parallax, factors that advise against a direct extrapolation to the *Gaia* RV sample. Further, the offset we use is in agreement with tests on particular sources in Stassun & Torres (2018) and Zinn et al. (2019). We employ the quality cuts suggested in section 8 of Schönrich et al. (2019). We furthermore require a parallax quality ratio $p/\sigma_p > 10$ and an additional cut on Galactic latitude of $b > 10°$. The resulting distribution of stellar loci can be found in Fig. 1.

4 A NEW WAVE PATTERN IN *GAIA* DR2

4.1 The pattern of radial motion versus angular momentum

We can now turn to the topic of this paper: a wave-like structure in the radial velocity component. This wave pattern has occasionally been found in studies of the phase-space properties of *Gaia* DR2, e.g. in fig. 1 of Fragkoudi et al. (2019) and the lower panel of fig. 13 in Laporte et al. (2019). However, it has mostly been pictured in the *R–V* plane, which obstructs that the most natural variable for its description is the angular momentum L_z. Studying the pattern as a function of L_z allows us to examine it very closely and even pin down a phase shift throughout our sample.

Fig. 2 shows the mean U_g velocity component in bins of angular momentum. To generate this plot, we ordered the sample in the angular momentum $L_z = RV_g$ of each star. For the well-populated region with L_z between 1600 and 2150 km s^{-1}, we then sliced the sample into bins of 20 000 stars each, while we use bins of 10 000 stars outside the core region in L_z. All data points are formally independent. However, in particular outside the core region in L_z, distance uncertainties will blur stars modestly along the x-axis. The magnitude selection in this sample strongly favours nearby stars, where *Gaia* parallaxes are very precise. The relative distance uncertainty distribution is provided in Fig. A2, and peaks strongly around 2 per cent. Systematic uncertainties will be of order 1 per cent in the near field and slightly larger for remote stars.

It is instantly evident from Fig. 2 that $\overline{U}_g$ varies with a wave-like pattern of a wavelength of about 300 kpc km s^{-1} and an amplitude of order 4 km s^{-1} in $\overline{U}_g$. The pattern lies on top of larger scale fluctuations that are of order 10 km s^{-1}, i.e. we see that stars with low angular momentum have a net outwards motion relative to the LSR. The general trend of $\overline{U}_g$ with R_g and hence L_z has been expected
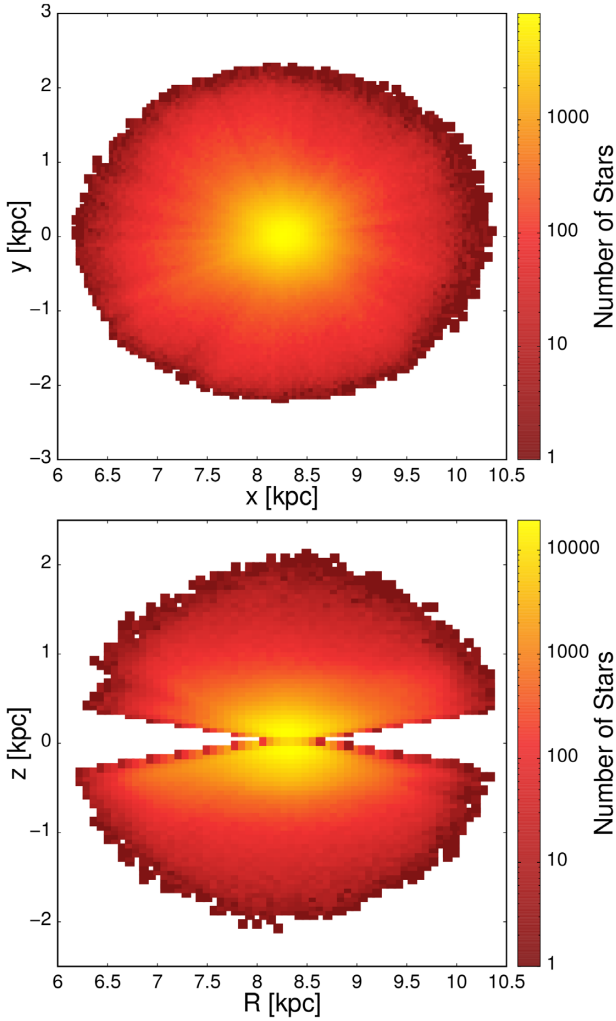
Figure 1. Geometry of the *Gaia* sample we used after introducing the various quality cuts explained in Section 3.

Figure 2. Mean radial velocity component $\overline{U}_g$ of all stars in the sample, when binned by angular momentum L_z. For each data point, 10 000 stars (20 000 stars for L_z between 1600 and 2150 km s^{-1}) were taken from the sample sorted in L_z. The error bars depict the Poisson noise in each bin, i.e. $\sigma_{U_g}/\sqrt{N}$, where N is the number of stars in each bin and σ_{U_g} its measured dispersion in U_g.

from prior models analysing the effects of the bar: resonances of the bar are not only identified with features like the Hercules stream (Dehnen 2000; Pérez-Villegas et al. 2017; Monari et al. 2019b) (which itself has a strong average radial motion outwards), but the bar is also expected to cause a significantly non-zero $\overline{U}_g$ all around the disc on its main resonances (Mühlbauer & Dehnen 2003), most notably the change of sign from negative to positive $\overline{U}_g$ shortly outside the outer Lindblad resonance due to the quadrupole moment of the bar. Similarly, we expect some imprints of the spiral arms both in $\overline{U}_g$ versus L_z and in $\overline{U}_g$ versus R (e.g. Monari, Famaey & Siebert 2016). However, the wave-like nature of the pattern in $\overline{U}_g$ is unexpected, and somewhat surprising. We can make out in total four peaks in $\overline{U}_g$, where the peak near the solar value of $L_z \sim 2070$ kpc is wider and has a different appearance. We also experimented with different sample sizes, but it appears impossible at current stage to resolve more extreme values of L_z.

The first two questions to ask are of course: How confined is this feature to the plane, and, given that we detect it in L_z only, how confined is it in Galactocentric radius? This is answered in Fig. 3. To create the top panel, we introduced the local vertical energy relative to a star moving with no vertical velocity in the mid-plane:

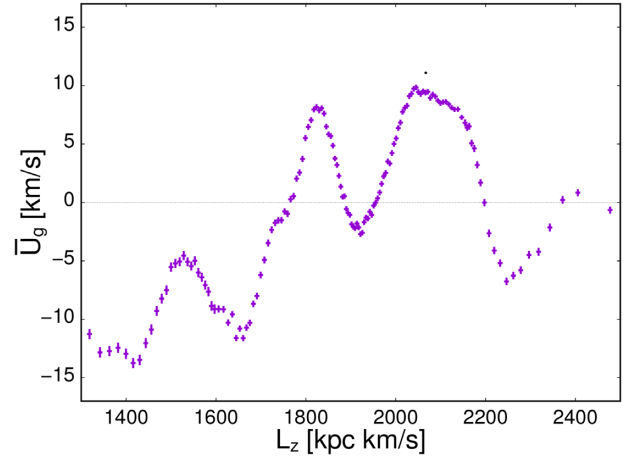$$E_z = \frac{1}{2}W^2 + \Phi(R, z) - \Phi(R, 0), \tag{1}$$

where $\Phi(R, z)$ is the galactic potential according to the mass model of McMillan (2017) at the position of the star, $\Phi(R, 0)$ is the potential at its projected position in the plane, and W^2 is the square of its vertical velocity component. Of course the vertical action would be a better conserved quantity, but E_z provides a straightforward ordering in vertical extent along each orbit. We can see that the pattern persists with little change towards larger E_z, even though the maximum vertical energy plotted here corresponds to a vertical velocity of $W \sim 49$ km s^{-1} or respectively orbits extending to $z \sim 1$ kpc altitude. In light of this stability, we expect the same result in vertical action. Curiously, the pattern slightly shifts in L_z with E_z: most prominently, the large peak around $L_z \sim 2100$ kpc km s^{-1} shifts to of order 80 kpc km s^{-1} lower L_z for large E_z values. Similar trends can be guessed for most of the remaining pattern, though the highest L_z feature hints at a slight rightward drift relative to the rest of the pattern, with the minimum of $\overline{U}_g$ around $L_z \sim 2250$ kpc km s^{-1} deepening somewhat towards larger E_z. The leftward drift can be expected if the peaks are physically connected to orbital resonances, since the orbital frequencies should show a slight drift downwards for vertically more extended orbits.

The middle and bottom panels of Fig. 3 show the sample in the L_z–V_g and L_z–R planes. Of course, both plots are closely related by $L_z = RV_g$. Lines of constant radius in the middle panel run from lower left to upper right. The strong selection bias of the sample towards the solar Galactocentric radius implies that we have a dearth of stars in the top-left and bottom-right corners of this plot. There is some dependence of the pattern on V_g. The most likely interpretation is that the wave pattern has some dependence on the orbital phase, although at current stage it is difficult to disentangle this completely from sample selection effects. The sample selection shows more strongly in L_z versus R (bottom panel). Again, there is a dependence on R, mostly in amplitude, but also with a surprising curving of the pattern at $R \sim 7.5$ kpc. A part of the amplitude dependence can be ascribed to the asymmetry in distance biases.

To get a better grip on the R dependence and other parameters, we repeat the plot of Fig. 2 in Fig. 4 when selecting different ranges in each parameter. The top-left panel of Fig. 4 shows $\overline{U}_g$ versus L_z for different bands of R. It is clear that for large R we have to lose all
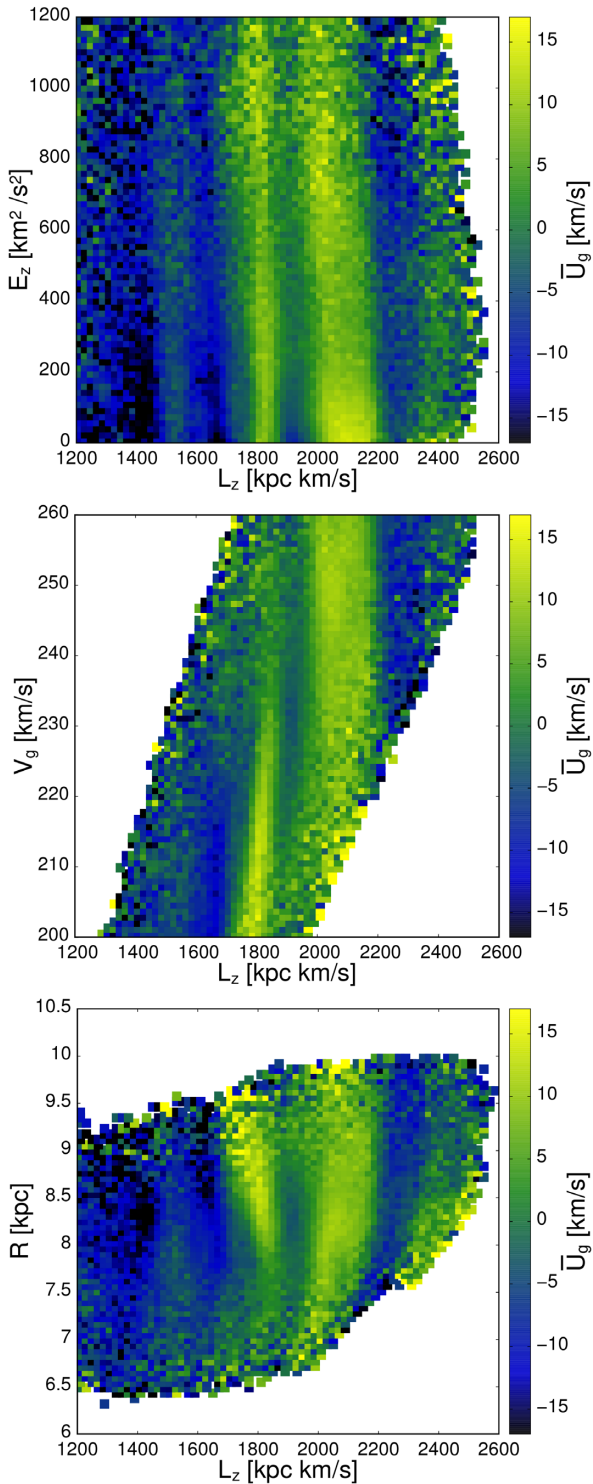
Figure 3. Mean radial velocity $\overline{U}_g$ marked by colour on the L_z–E_z plane (top panel), the L_z–V_g plane (middle panel), and L_z–R (bottom panel). For each data bin, we required a minimum star number of 10.

This effect is also asymmetric in R and in L_z, which we make clear with an example: at large distances of order 2 kpc, a realistic *Gaia* parallax error of $\sigma_p \sim 0.05$ mas results in a distance uncertainty of ~ 10 per cent. In direction towards the GC, a distance error affects the L_z measurement twice in the same direction: a star with $(R, V_g) = (6 \text{ kpc}, 200 \text{ km s}^{-1})$ will, if we underestimate its distance by 10 per cent, be measured at $(R', V'_g) \sim (6.23 \text{ kpc}, 205 \text{ km s}^{-1})$ or respectively will have moved about a quarter wavelength of the wave pattern in L_z. If we measure a star with high $V_g > 250$ km s^{-1} in the same place, the V_g velocity error will change sign and counteract the error in R. Analogously, errors for stars observed at large radii (towards the Galactic anticentre) with low V_g tend to cancel, while they will be additive for stars with large $V_g > V_{g,\odot}$. This explains the main trends in $\overline{V}_g$ and R. We have formally good data for low L_z and low V_g, but in particular at small R, the additive error budget will smear out the pattern in L_z. Similarly, the wave pattern disappears at large R and small R, explaining the loss of signal at extreme values. In short, while our data sets have been optimised for unbiased distances, we still face a loss of signal to random errors.

The bottom-left panel of Fig. 4 shows the wave-like pattern sliced in different bins of z. Focusing e.g. on the two most extreme altitude bands at $0.6 < |z|/\text{kpc} < 1$ versus the rest of the sample, we can see that the pattern shifts symmetrically with increasing altitude. Note that the Galactic latitude cut of $b > 10°$ implies that for small $|z|$ our sample is restricted to near solar radius stars. However, the quality difference with random errors to first order only affects the measured amplitude, so the consistent pattern/phase shift with $|z|$ is real. Further, the symmetry in z of the shift argues against systematic distance errors. The left shift of the pattern can quite straightforwardly be attributed to the slower orbital frequencies for stars reaching high altitude.

The phase shift with $|z|$ is consistent with the bottom-right panel in Fig. 4, where we separate the sample in the vertical energy E_z of the stars. Again, with increasing vertical extent of the orbits, the pattern exhibits a constant shift to lower angular momentum. The shift is clearly detectable through the entire L_z range. We find again that with increasing E_z the signal tends to get weaker. Yet, again at least some of this loss of amplitude will be caused by the increasing distance uncertainties.

The top-right panel tries to resolve the ϕ dependence of the wave-like structure. This is particular interesting, since it can give us clues about the perturbation causing the pattern and the wavenumber of this perturbation. The phase shift with ϕ is already visible to the naked eye. In particular, the left prominent peak shifts systematically to the left with increasing ϕ, i.e. resembles a trailing pattern. Again, measurements at large $|\phi|$ are ridden with distance uncertainties, since all their stars are at the fringes of our quality limits, but this is a promising start for a further investigation. Unlike $|z|$, where all peaks shifted consistently, the behaviour in ϕ indicates that this is a superposition of at least two causes/modes with different wavenumbers.

4.2 Constraining the phase shift

Just having seen the phase shift of the pattern with Galactic azimuth ϕ, we attempt to quantify it and to derive the wavenumber m. Any fit will be far from perfect, since the changing distance error distribution will increasingly wash out the wave pattern towards larger $|\phi|$. The idea is that if we find a half-way decent fit function for a local, well-constrained part of the sample that also gives reasonable fits for the adjacent regions, the alignment of data and the fit should be enough to pick out the average amount of phase
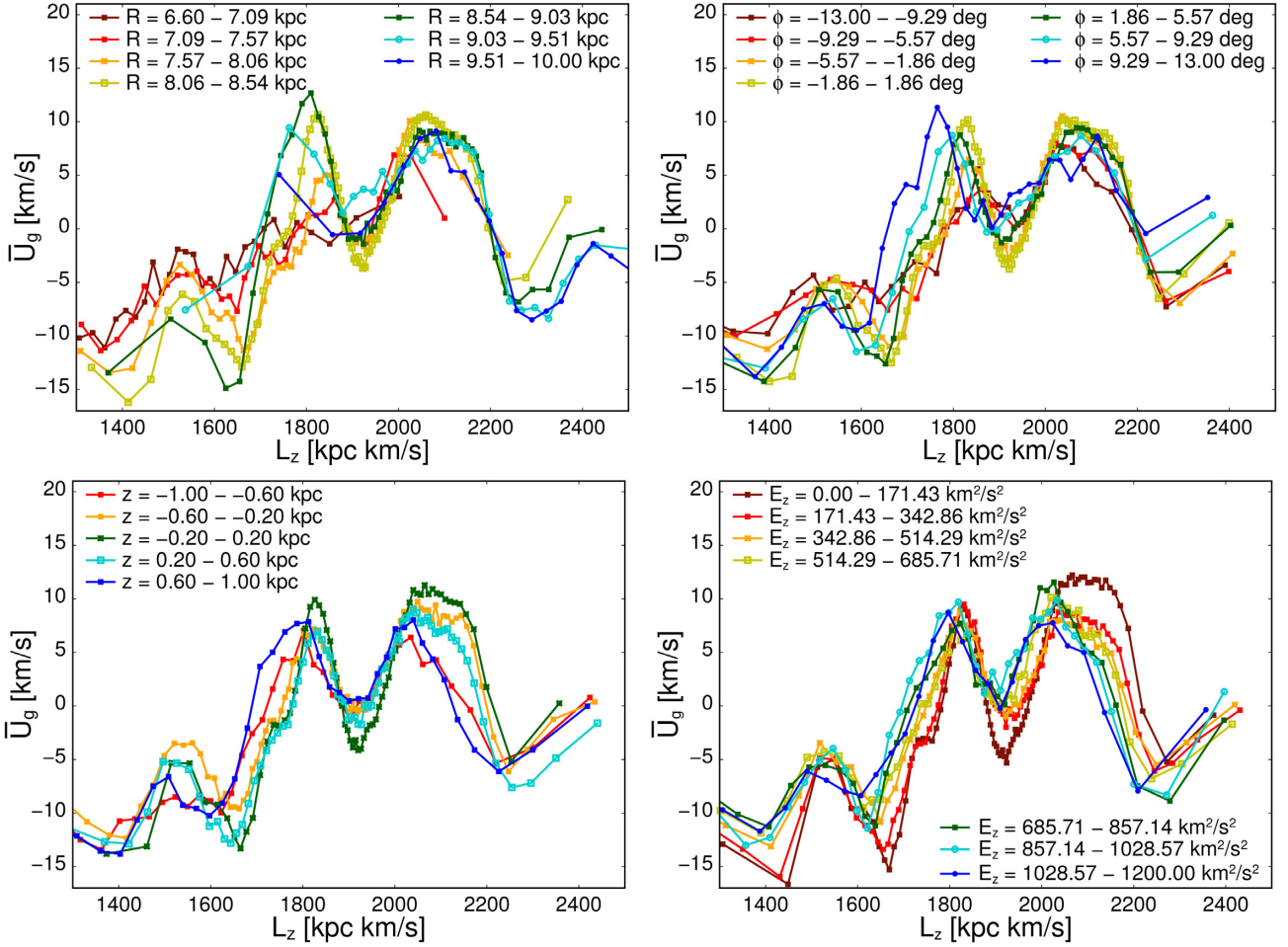
signal at low angular momenta, and for small R we have virtually no stars with large angular momentum. As indicated in the previous paragraph, for small $R < 7.5$ kpc, the wave pattern appears to get consistently weaker, especially in the low-L_z range. However, this range is plagued by the larger uncertainties for remote stars, which blur out the peaks in $\overline{U}_g$.

Figure 4. We use the same data as in Fig. 2, but divide the sample into equal width regions in Galactocentric radius R (top-left panel), Galactic azimuth ϕ (top-right panel), vertical altitude z (bottom-left panel), and vertical energy E_z (bottom-right panel).

shift, even with imperfect parameters for amplitude and wavelength in L_z. If we then assume that we have made a reasonable choice for the wavelength of the fit function, we can estimate the wavenumber m from the slope of the fit in δL_z versus ϕ by dividing it by the wavelength.

To find the best-guess fit function, we picked a subsample restricted to 8.06–8.55 kpc in Galactocentric radius and $-1.86°$ to $1.86°$ in azimuth, which is depicted in the top panel of Fig. 5. As can be seen from the blue line in the plot, the pattern is well fitted by a superposition of a fast and a slow wave:

$$\overline{U}_g(L_z) = \sum_{i=1}^{2} A_i \sin\left((L_z + \delta_{L_z,i}) \cdot \frac{2\pi}{\lambda_i}\right) + t. \tag{2}$$

We held constant our amplitudes $A_1 = 7.0\,\mathrm{km\,s^{-1}}$, $A_2 = 8.0\,\mathrm{km\,s^{-1}}$ and wavelengths $\lambda_1 = 285\,\mathrm{kpc\,km\,s^{-1}}$, $\lambda_2 = 1350\,\mathrm{kpc\,km\,s^{-1}}$, $\delta_{L_z,2} = 1010\,\mathrm{kpc\,km\,s^{-1}}$, and $t = -2.877\,\mathrm{km\,s^{-1}}$ and varied the phase $\delta_{L_z,1}$ for azimuthal slices of width $1.68°$, fitting to the full sample in each range of ϕ. Fixing the $\delta_{L_z,2}$ of the slowly varying wave is a matter of fitting hygiene. The pattern is not a perfect sinusoid, and biases and uncertainties wash it out near the rim of the sample. Leaving all parameters free would lead to wild jumps in parameters, with the fitted function aligning with other features than the main ridges/troughs identified here. Since the main objective of

this fit is to constrain the phase shift of the specific extrema that seem to be guided by the same wavenumber, and lacking for now a comprehensive physical model that reproduces the precise shape of the pattern, we allow ourselves the simplification of fitting only the phase of the short-wavelength wave.

The lower panel of Fig. 5 shows the fitted $\delta_{L_z,1}$ over the average azimuth in their bin and assumed a linear fit to derive the average phase shift in $\mathrm{kpc\,km\,s^{-1}\,rad^{-1}}$ as slope of that fit. We found that taking the whole sample into account resulted in a slope of $(97 \pm 32)\,\mathrm{kpc\,km\,s^{-1}\,rad^{-1}}$.

To help a further analysis of the phase shift, Fig. 6 shows the complete azimuthal plane of our sample. It is clear that the two prominent maxima behave differently with the left one shifting more rapidly to large L_z for small azimuth. This is also the main problem when fitting, as the maxima nearly coincide at small ϕ. Together with the increased distance uncertainties, fits at large $|\phi|$ become unreliable. The peak near $L_z \sim 2100\,\mathrm{kpc\,km\,s^{-1}}$ shows again a clearly different behaviour from the rest of the pattern, with a significantly lower phase shift in ϕ. We therefore refitted equation (2), while excluding stars with $1950 < L_z\,(\mathrm{kpc\,km\,s^{-1}}) < 2250$. The resulting phase shifts are shown with bright red error bars in the bottom panel of Fig. 5. The best-fitting linear slope for these (shown with the green line) is $\mathrm{d}L_z/\mathrm{d}\phi = (202 \pm 22)\,\mathrm{kpc\,km\,s^{-1}\,rad^{-1}}$. Again, the different results for the phase shift after excluding the broad peak in $\overline{U}_g$ from
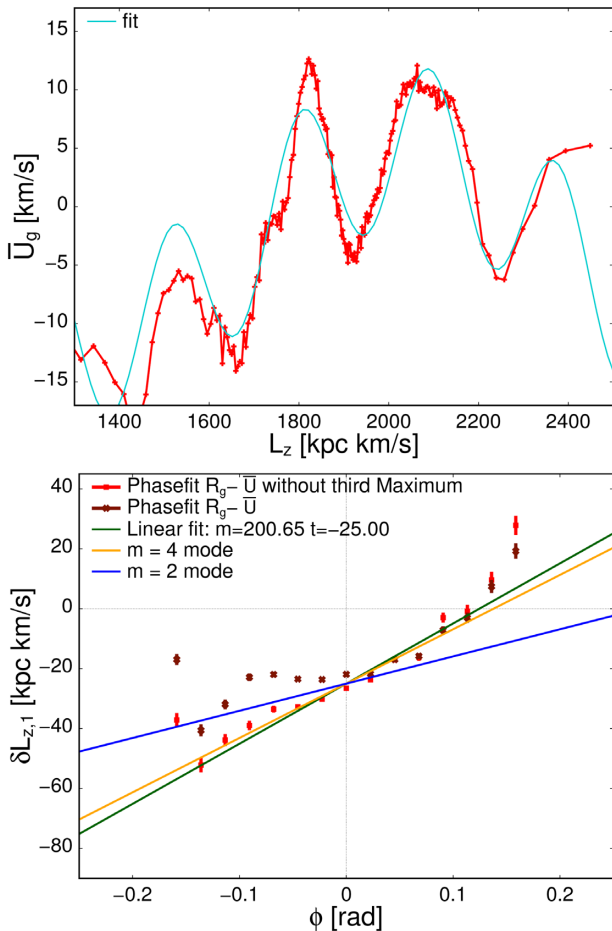
Figure 6. The mean U_g velocity component in bins of ϕ and L_z. We can see the systematic phase shift of the single peaks and troughs. It becomes quite clear that the most prominent peak appears to have a lower wavenumber m than the rest of the pattern. To guide the eye, we have entered lines for phase shifts in L_z with $m = 4$ to the peak at $L_z(\phi = 0) = 1820 \, \mathrm{kpc \, km \, s^{-1}}$ and $m = 2$ as well as a vertical dot–dashed line for the wide peak at $L_z(\phi = 0) = 2100 \, \mathrm{kpc \, km \, s^{-1}}$. In addition to the main maxima, we have also introduced lines corresponding to wavenumbers of $m = 4$ for three more extrema (dashed lines).

4.3 Connecting to the vertical wave pattern

In Fig. 7, we show the $\overline{U}_g$–L_z pattern overlaid with the same evaluation for $\overline{W}$ versus L_z. We further introduce the guiding centre radius $R_g = L_z/V_c$, where for the sake of simplicity and easy reproduction we assume a flat rotation curve with $V_c = 238 \, \mathrm{km \, s^{-1}}$. We duplicated our analysis using the more realistic rotation curve by McMillan (2017). Not surprisingly, the resulting differences are negligible: using a different $V_c = 233.1 \, \mathrm{km \, s^{-1}}$ just shifts the pattern proportionally in L_z; the change of V_c with R is much smaller than the width of the observed structures and smaller than the systematic uncertainties from the distance measurements.

We instantly see that the vertical wave pattern detected by Schönrich & Dehnen (2018) appears to be strongly correlated with the $\overline{U}_g$ wave discussed in this paper: the wave peaks in $\overline{W}$ appear to line up with the outer troughs of the $\overline{U}_g$ wave. This could be a mere coincidence, but the degree of alignment suggests rather a physical correlation. As the amplitude in $\overline{W}$ is a factor ~ 5, our sample could not yield a reliable signal for $\overline{W}$ versus ϕ to track the phase shift.

Many hypotheses can be drawn for this alignment. Of course, a common origin could be suggested if both the radial and the vertical wave originate from the same dwarf galaxy impact (e.g. Binney & Schönrich 2018). This may be related to the phase-space spiral being observed in both vertical and radial motion, but on the other hand, in a naive picture, it is not clear why the alignment is then not removed by different frequencies in radial versus vertical oscillation. The same complication would arise if one wanted to adopt the less favoured explanation of the phase-space spiral by a bar buckling event (Khoperskov et al. 2019). Monari et al. (2016) showed that the presence of spiral arms leads to vertical breathing modes aligned with the radial mean motion, which, however, include a vertical velocity field of odd parity that is not observed here. Another prediction has been made in Masset & Tagger (1997). In their paper, the authors predict that near an outer Lindblad resonance a spiral wave should interact with the galactic warp to produce a

Figure 5. Top panel: Fit of function (2) to a data sample restricted to a box of radial width of 0.49 kpc and angular width of 3.7° centred around the Sun. Bottom panel: The phase shift δ_1 via equation (2) with increasing azimuth. We compare two fits, one for a sample including the whole L_z range and one fit where we exclude the angular momentum region of the third peak between 1950 and 2250 kpc km s^{-1}.

the sample indicate that two causes with different wavenumbers are responsible for the pattern. If we believe the wavelength of the fit function, the phase shift translates to a wavenumber $m = 4.4 \pm 0.5$, suggesting an $m = 4$ perturbation.

We tried to make this more evident by introducing lines in Fig. 6 depicting different linear phase shifts dL_z/dϕ at the positions of the maxima. We can see that indeed the maximum near $L_z \sim 1850 \, \mathrm{kpc \, km \, s^{-1}}$ is well approximated by a phase shift of $180 \, \mathrm{kpc \, km \, s^{-1} \, rad^{-1}}$ (consistent with an $m = 4$ mode). The broad peak around $L_z \sim 2100 \, \mathrm{kpc \, km \, s^{-1}}$ is too wide to allow for a firm statement. It is incompatible with the large dL_z/dϕ, but consistent with any scenario between a moderate dL_z/d$\phi = 90 \, \mathrm{kpc \, km \, s^{-1} \, rad^{-1}}$ (solid line, consistent with an $m = 2$ mode) or even a constant phase (dot–dashed line). For three other, less prominent extrema, we also introduced dashed lines corresponding to a wavenumber of $m = 4$. Whereas the right minimum is not incommensurable with this phase shift, the proximity to the wide maximum to its left renders it hard to make a definite claim for its phase shift. The two extrema at low L_z, however, are again well fitted by the $m = 4$ mode.

We conclude that the observed pattern is consistent with a superposition of two trailing patterns in Galactic azimuth.
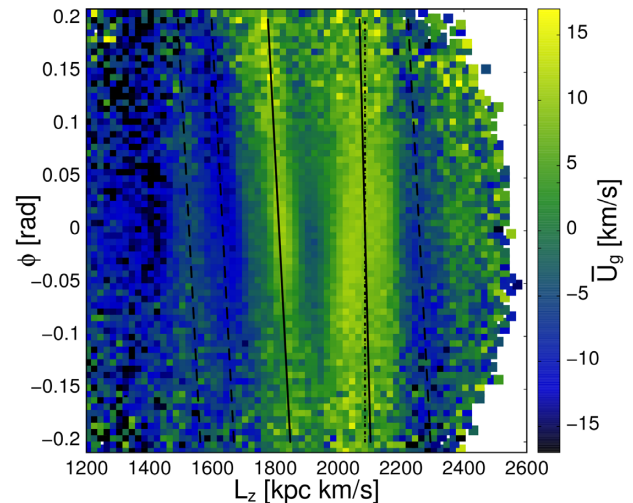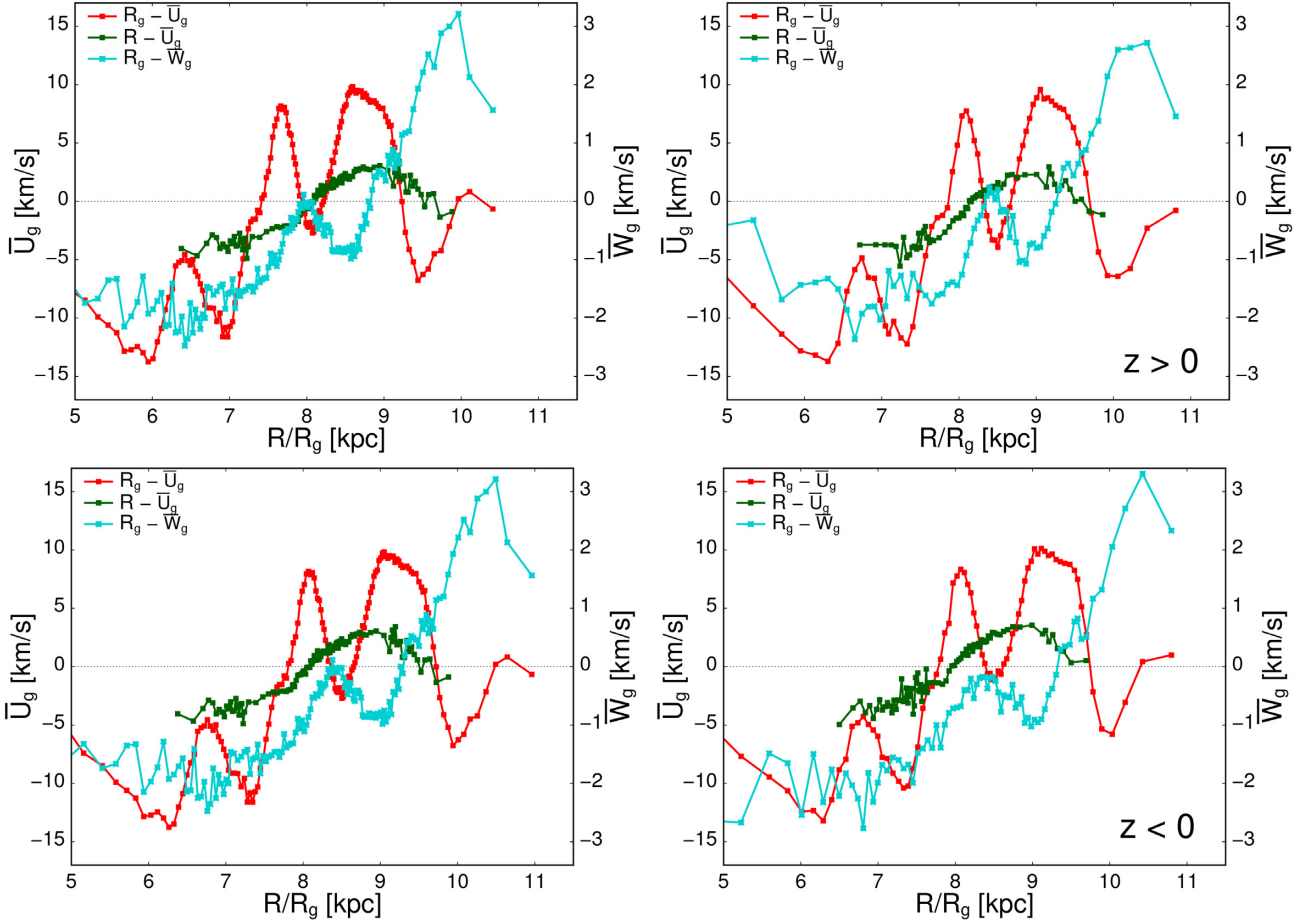
Figure 7. Comparison of the signal in R–$\overline{U}_g$ and the one in R_g–$\overline{U}_g$ and R_g–$\overline{W}$. To highlight the alignments of the extrema and make the weaker R_g–$\overline{W}$ signal better visible, we stretched this graph by a factor of 5. The two panels on the left use the same data, but the lower one accounts for asymmetric drift effects in the derivation of L_z by taking $R_g = L_z/\overline{V}_g = L_z/(226\,\mathrm{km\,s^{-1}})$ instead of $R_g = L_z/V_{c,\odot} = L_z/(238\,\mathrm{km\,s^{-1}})$. The panels on the right again use the same data as the lower left panel for positive z (upper right panel) and negative z (lower right panel).

coupled horizontal and vertical wave. However, this effect should again be antisymmetric around the Galactic plane.

We thus examine the signals separated by galactic hemisphere in Fig. 7. We find a mild difference of the vertical and radial velocity patterns above and below the Galactic plane, with a mildly stronger overlap of the extrema in $\overline{U}_g$ and $\overline{W}$ for positive z. While $\overline{U}_g$ is slightly decreased in the Northern hemisphere (when taken with respect to R as well as to L_z), $\overline{W}$ is shifted upwards in our plot and shows a borderline significant third peak near $R_g \sim 7.2$ kpc. The general alignment is, however, clearly visible for both hemispheres.

Fig. 7 also compares the $\overline{U}_g$ versus R pattern to the $\overline{U}_g$–L_z dependence. Trends of $\overline{U}_g$ with R have been predicted at least since the time of *Hipparcos* (Mühlbauer & Dehnen 2003). Later, hints for a gradient in $\overline{U}_g$ versus R have been found e.g. by Siebert et al. (2012) in RAVE data. They were explained by Faure, Siebert & Famaey (2014), who showed with a 3D test particle simulation that a spiral structure can be responsible for the observed pattern. Liu et al. (2018) continued along the line of argumentation by Mühlbauer & Dehnen (2003) and suggested that a bar is responsible for the dependence of $\overline{U}_g$ on R. The simple pattern that we find in $\overline{U}_g$ versus R very strongly resembles and qualitatively agrees with this prediction from Mühlbauer & Dehnen (2003). We also note that the $\overline{U}_g$ versus R dependence in Fig. 7 resembles the findings in fig. 12 of Gaia Collaboration (2018b). It is also evident that this dependence is

mostly a washed-out (by epicyclic motions of the orbits around their guiding centre) version of what we see in L_z. To make this clearer, we repeat the plot of the top panel of Fig. 7 in the bottom panel, with one change: instead of using the assumed circular velocity $V_c = 238\,\mathrm{km\,s^{-1}}$ to translate L_z to R_g, we add an asymmetric drift and use $\overline{V}_g = 226\,\mathrm{km\,s^{-1}}$ to translate. Unsurprisingly, this results in a good agreement between the patterns in L_z and R. A plot showing that the washing out of the pattern is also observed in radial against azimuthal velocity can be found in Fig. A5.

5 CONCLUSION

We have for the first time closely examined a prominent wave-like pattern in mean radial velocities $\overline{U}_g$ versus angular momentum L_z in the RV subsample of *Gaia* DR2. The amplitude of the pattern is of order $4\,\mathrm{km\,s^{-1}}$ with a wavelength of about $285\,\mathrm{km\,s^{-1}}$ kpc in L_z or ~ 1.2 kpc in guiding centre radius R_g. To our knowledge, this pattern has not been directly predicted by any Galaxy model, though of course the offsets in $\overline{U}_g$ predicted in the V_g–$\overline{U}_g$ plane by papers like Monari et al. (2019b) for distinct entities like the Hercules stream should be related to our finding.

The structure is evidently not bound to a single Galactocentric radius R. We can detect it in a region of ~ 7–10 kpc, i.e. a band of ~ 3 kpc around the Sun. There is a slight drift of the ridges towards smaller L_z for small V_g; however, the dependence of L_z on V_g and R

makes it hard to raise definite claims for the evolution of the pattern with these quantities.

The wave-like structure is not limited to kinematically cold thin-disc stars. We binned the sample in the local vertical energy E_z and found that the wave-like pattern persists to stars with $E_z \sim 1200\,(\text{km\,s}^{-1})^2$, i.e. stars with orbits passing beyond thick-disc altitudes $|z| > 1$ kpc. For these kinematically very hot populations, the amplitude appears to be roughly half of the amplitude for kinematically cold stars, but this decrease is likely overestimated due to larger distance uncertainties blurring the pattern. Towards larger E_z, the pattern shifts to the left, i.e. smaller L_z with a trend of about $0.05\,\text{kpc\,km\,s}^{-1}/(\text{km\,s}^{-1})^2$. This is likely connected to the slower radial frequencies of stars at higher altitudes.

Most interestingly, the *Gaia* data set is sufficiently extended that we can detect the slope of the ridges against the Galactic angle ϕ. Without specifying a model, we can thus draw conclusions on the physical cause of the pattern: All ridges tend towards lower L_z for larger ϕ, consistent with a trailing pattern in Galactic azimuth. However, there is a clear deviation with the peak in positive U_g near $L_z \sim 2100\,\text{km\,s}^{-1}$ kpc showing only about half the change of the rest of the pattern. If we filter out this peak from our analysis, the slope of the remaining pattern in L_z versus ϕ is consistent with an $m = 4$ wavenumber.

Hence, it is logical to associate this uniformly shifted part with an $m = 4$ excitation, possibly caused by the spiral pattern of the Milky Way or higher order ($m \geq 4$) contributions to the bar potential. The non-sloped (or only slightly sloped) broad peak hints to a connection with a bar resonance, however, to which depends on the bar pattern speed. A fast bar with a pattern speed of $\sim 55\,\text{km\,s}^{-1}\,\text{kpc}^{-1}$ as, for example, advocated for in Dehnen (2000) and Antoja et al. (2014) would have its outer Lindblad resonance in this region. However, a proposed much slower pattern speed of $39\,\text{km\,s}^{-1}\,\text{kpc}^{-1}$ (e.g. Pérez-Villegas et al. 2017; Monari et al. 2019b) connects it rather to the corotation resonance. In this area falls also the highly debated origin of the Hercules moving group, which has often been associated with the outer Lindblad resonance (Dehnen 2000), whereas some recent studies suggest a corotation resonance origin (D'Onghia & Aguerri 2019; Monari et al. 2019a). There are none the less no properties of the pattern that favour one or the other bar model.

Comparing the $\overline{U}_g$ versus R_g pattern to the similar pattern in $\overline{U}_g$ versus R, we find that the overall peak in $\overline{U}_g$ versus R (which is already present in the analysis of Gaia Collaboration 2018b) around $R \sim 8.8$ kpc is in line with the $\overline{U}_g$ versus R_g pattern being smeared out by epicyclic motions, once we account for the fact that the latter is shifted towards slightly larger values of R_g by the asymmetric drift.

Last, we compared the newly found U_g versus L_z pattern to the wave-like structure found by Schönrich & Dehnen (2018) in DR1. This pattern is still present in *Gaia* DR2, but its wavelength in L_z is longer than the wavelength of the radial velocity pattern. The two peaks in W versus L_z clearly visible in this selection fall roughly in the region of two troughs of L_z. There is a hint of a third peak in $\overline{W}$ coinciding with the lowest $\overline{U}_g$ trough in L_z, particularly visible in the northern galactic hemisphere.

ACKNOWLEDGEMENTS

REFERENCES

Antoja T. et al., 2014, A&A, 563, A60
Antoja T. et al., 2018, Nature, 561, 360
Arenou F. et al., 2018, A&A, 616, A17
Bergemann M. et al., 2018, Nature, 555, 334
Binney J., Schönrich R., 2018, MNRAS, 481, 1501
Bland-Hawthorn J. et al., 2019, MNRAS, 486, 1167
Cropper M. et al., 2018, A&A, 616, A5
Darling K., Widrow L. M., 2018, MNRAS, 484, 1050
Dehnen W., 1998, AJ, 115, 2384
Dehnen W., 2000, AJ, 119, 800
D'Onghia E., Aguerri J. A. L., 2019, preprint (arXiv:1907.08484)
D'Onghia E., Madau P., Vera-Ciro C., Quillen A., Hernquist L., 2016, ApJ, 823, 4
Drimmel R., Spergel D. N., 2001, ApJ, 556, 181
Drimmel R., Smart R. L., Lattanzi M. G., 2000, A&A, 354, 67
Faure C., Siebert A., Famaey B., 2014, MNRAS, 440, 2564
Fragkoudi F. et al., 2019, MNRAS, 488, 3324
Gaia Collaboration, 2016a, A&A, 595, A1
Gaia Collaboration, 2016b, A&A, 595, A1
Gaia Collaboration, 2018a, A&A, 616, A1
Gaia Collaboration, 2018b, A&A, 616, A11
Gillessen S., Eisenhauer F., Trippe S., Alexander T., Genzel R., Martins F., Ott T., 2009, ApJ, 692, 1075
Khoperskov S., Di Matteo P., Gerhard O., Katz D., Haywood M., Combes F., Berczik P., Gomez A., 2019, A&A, 622, L6
Laporte C. F. P., Johnston K. V., Gómez F. A., Garavito-Camargo N., Besla G., 2018, MNRAS, 481, 286
Laporte C. F. P., Minchev I., Johnston K. V., Gómez F. A., 2019, MNRAS, 485, 3134
Lindegren L. et al., 2018, A&A, 616, A2
Liu C., Xu Y., Wang H., Wan J., 2018, in Chiappini C., Minchev I., Starkenburg E., Valentini M., eds, Proc. IAU Symp. 334, Rediscovering Our Galaxy. Cambridge Univ. Press, Cambridge, p. 109
McMillan P. J., 2017, MNRAS, 465, 76
Masset F., Tagger M., 1997, A&A, 318, 747
Monari G., Famaey B., Siebert A., 2016, MNRAS, 457, 2569
Monari G., Famaey B., Siebert A., Bienaymé O., Ibata R., Wegg C., Gerhard O., 2019a, preprint (arXiv:1908.01318)
Monari G., Famaey B., Siebert A., Wegg C., Gerhard O., 2019b, A&A, 626, A41
Mühlbauer G., Dehnen W., 2003, A&A, 401, 975
Pérez-Villegas A., Portail M., Wegg C., Gerhard O., 2017, ApJ, 840, L2
Perryman M. A. C. et al., 1997, A&A, 323, L49
Poggio E. et al., 2018, MNRAS, 481, L21
Reylé C., Marshall D. J. Robin A. C., Schultheis M., 2009, A&A, 495, 819
Sartoretti P. et al., 2018, A&A, 616, A6
Schönrich R., 2012, MNRAS, 427, 274
Schönrich R., Aumer M., 2017, MNRAS, 472, 3979

Schönrich R., Dehnen W., 2018, MNRAS, 478, 3809
Schönrich R., Binney J., Dehnen W., 2010, MNRAS, 403, 1829
Schönrich R., Binney J., Asplund M., 2012, MNRAS, 420, 1281
Schönrich R., McMillan P., Eyer L., 2019, MNRAS, 487, 3568
Seabroke G., Ciucă I., Cropper M., Kawata D., Baba J., Grand R. J. J., Hunt J. A. S., 2018, MNRAS, 479, L108
Siebert A. et al., 2012, MNRAS, 425, 2335
Stassun K. G., Torres G., 2018, ApJ, 862, 61
Trick W. H., Coronado J., Rix H.-W., 2019, MNRAS, 484, 3291
Weinberg M. D., 1995, ApJ, 455, L31
Xu Y., Newberg H. J., Carlin J. L., Liu C., Deng L., Li J., Schönrich R., Yanny B., 2015, ApJ, 801, 105
Zinn J. C., Pinsonneault M. H., Huber D., Stello D., 2019, ApJ, 878, 136

APPENDIX A: SAMPLE SELECTION AND QUALITY CUTS

We dedicate this appendix to some further quality tests in order to ascertain the significance of our findings and test for possible systematic effects. First, we want to make sure that the found pattern in L_z–$\overline{U}_g$ is not dependent on the choice of assumptions on parallax error $\delta\sigma_p$ and parallax bias δ_p in *Gaia* DR2. In the main text, we used exclusively the sample with $\delta\sigma_p = 0.043$ mas and $\delta_p = 0.054$ mas. Fig. A1 demonstrates that choosing any sample has only marginal consequences for the derived pattern of $\overline{U}_g$ versus L_z, with a minor deviation for very small L_z in the third sample, which uses $\delta\sigma_p = 0$ and $\delta_p = 0.048$ mas. This is easily understood, since the lack of an additional error term in σ_p allows for a further extent of the sample under our quality cut $p/\sigma_p > 10$. We also note that this sample has to be treated with caution, since there is good evidence that the *Gaia* pipeline values for σ_p are underestimated.

Fig. A2 shows the distribution of the standard deviation of the distances to estimated distance ratio, to help the reader assess the impact of distance uncertainties on our results. The relative error $\sigma_s/\bar{s}$ of the expected distance $\bar{s}$ peaks at around 2 per cent. The quality cut $p/\sigma_p > 10$ of course results in a similar cut-off in $\sigma_s/\bar{s}$,
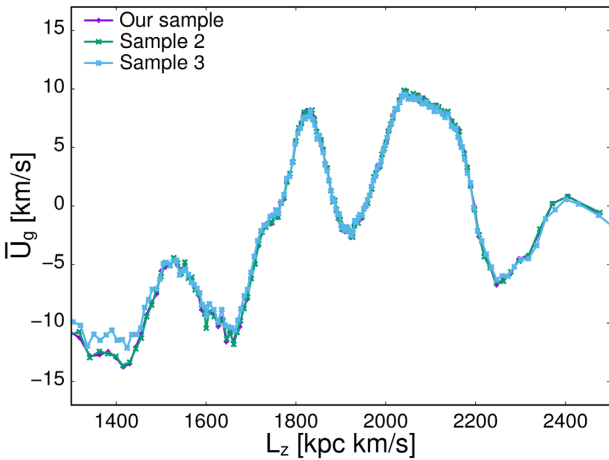

Figure A2. Distribution of distance standard deviation over estimated distance for our sample after applying the quality cuts.

Figure A3. Comparison of the L_z–$\overline{U}_g$ pattern for different quality cuts in parallax over parallax error.

removing basically all stars with an estimated relative distance uncertainty greater than ∼11 per cent. The strong peak at small relative errors results from the magnitude-based selection in the *Gaia* RV subset, which strongly favours nearby stars. Note that the large distance uncertainties are of course found predominantly near the distant rim of our sample, the consequence of which we will examine further below.

It is important to consider how different demands on the quality of our sample affect the pattern. Throughout this work, we required (in addition to the quality cuts suggested in section 8 of Schönrich et al. 2019) a quality cut $p/\sigma_p > 10$. However, as Fig. A3 shows, different p/σ_p ratios have only very little influence on the strength of the pattern, with a slightly lower amplitude for lower quality requirements due to random errors.

As our discussed wave pattern proved especially hard to resolve in radius, we repeat the plot of the bottom panel of Fig. 3 in the upper panel of Fig. A4 with a parallax cut of $p/\sigma_p > 20$. We find that the radial data range is strongly affected by this requirement and that the peculiar bent in $\overline{U}_g$ for radii of ∼7.5 kpc cannot be resolved anymore. It is thus likely that a definitive analysis of this has to await *Gaia* DR3.

As discussed in Section 4.1, any pattern in the angular momentum should be increasingly washed out with increasing L_z uncertainty

Figure A1. Comparison of the L_z–$\overline{U}_g$ pattern for three data samples derived from *Gaia* data. Sample 2 also increases the parallax error $\sigma_p = \sqrt{\sigma_p'^2 + (\delta\sigma_p)^2}$ by $\delta\sigma_p = 0.043$ mas but corrects for an parallax offset $\delta p = \sigma_p$. Sample 3 only includes a parallax offset $\delta p = 0.048$ mas and no increase of the parallax error, i.e. $\delta\sigma_p = 0$. It is the most extended, but also the one with the largest relative uncertainties (the formal error uncertainty in that sample is up to a factor 2 smaller for most stars), so the signal in L_z will be a little more blurred. Further information on the derivation of our samples can be found in Schönrich et al. (2019).
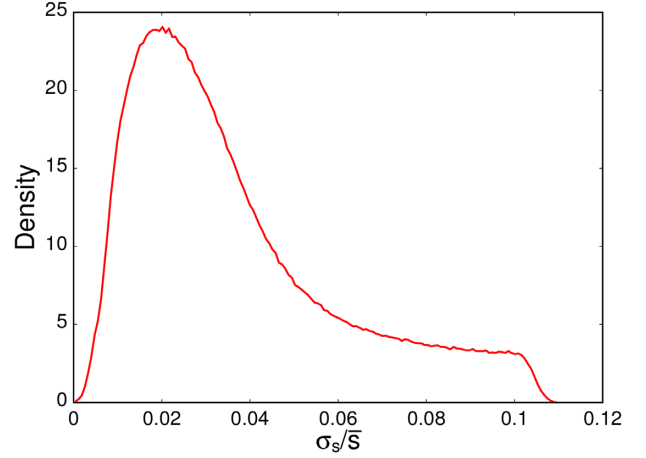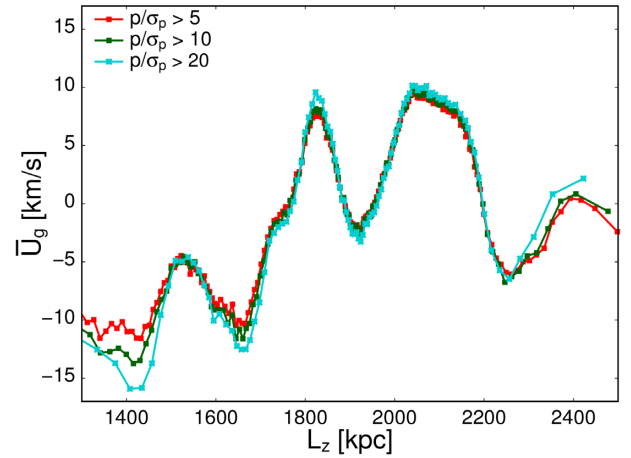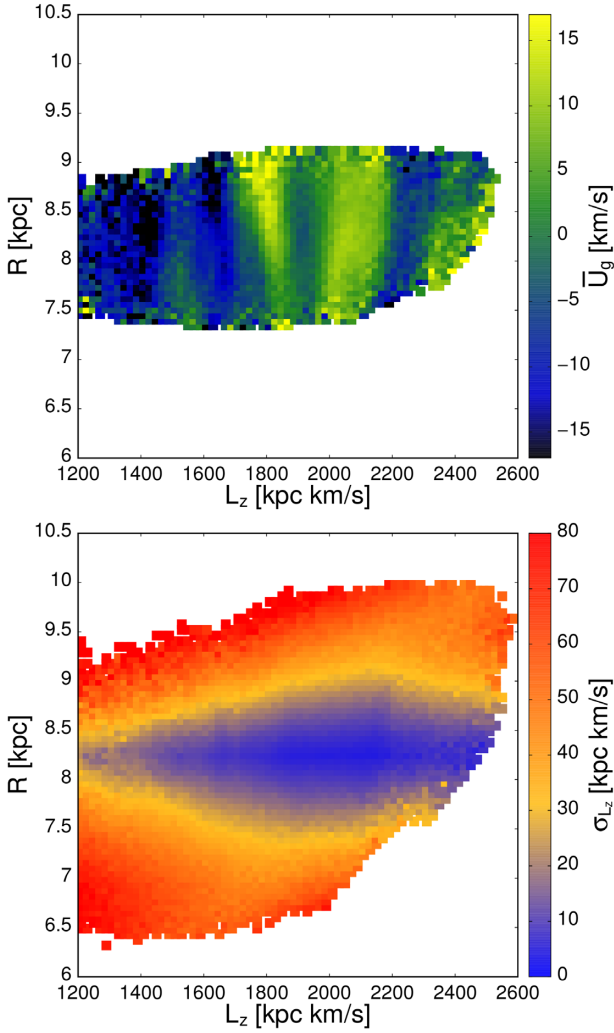
Figure A4. Upper panel: Same plot as in the lower panel of Fig. 3 but with the higher quality requirement of parallax over parallax error bigger than 20. Lower panel: Estimated standard deviation of the angular momentum L_z from the distance error.
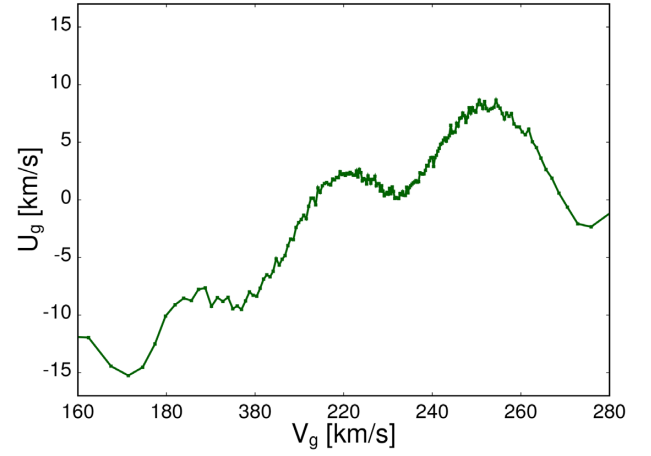

Figure A5. Azimuthal versus radial velocity for the sample with $p/\sigma_p > 10$.

and should nearly disappear for an uncertainty exceeding roughly half a wavelength of the pattern. Stars at small R are particularly prone due to the additive effect of a distance error on both R and V_g in this region. We tried to estimate the error in L_z from the distance uncertainty by taking $\sigma_{L_z} \approx \sigma_s \cdot dL_z/ds$, where s is the expected distance to the star and σ_s the standard deviation of the distance probability distribution. The resulting pattern of the averaged σ_{L_z} (in quadrature) in the L_z–R plane can be found in the lower panel of Fig. A4. Consistent with our findings in the main text, in the red regions of this figure we do not expect to still find a clear $\overline{U}_g$ signal, as $\sigma_{L_z} > 70\,\mathrm{kpc\,km\,s^{-1}}$ exceeds one quarter of the wavelength of the observed pattern.

Following the discussion in Section 4.3 that a washed-out version of the discussed wave pattern can be observed also in radial velocity versus radius (Fig. 7), Fig. A5 shows that the same effect takes place if we consider U_g against the azimuthal velocity V_g instead of the angular momentum. The remaining pattern, however, follows the behaviour of L_z–R yet more closely.

This paper has been typeset from a TeX/LaTeX file prepared by the author.